Erosion threshold of sand–mud mixtures

Walter Jacobs [a,b,*], Pierre Le Hir [c], Walther Van Kesteren [d], Philippe Cann [c]

[a] Royal Boskalis Westminster N.V., P.O. Box 43, 3350 AA, Papendrecht, the Netherlands
[b] Delft University of Technology, Faculty of Civil Engineering and Geosciences, Hydraulic Engineering Section, P.O. Box 5048, 2628 CN, Delft, the Netherlands
[c] IFREMER, centre de Brest, BP 70, 29280 Plouzané, France
[d] Deltares, P.O. Box 177, 2600 MH, Delft, the Netherlands

ARTICLE INFO

ABSTRACT

Results of a large number of erosion tests on artificially generated and relatively dense sand–mud mixtures are presented. Soil sample compositions are varied concerning clay–silt and sand–silt ratio, and clay mineralogy. The experimental set-up consists of a re-circulating small-scale rectangular erosion flume with unidirectional flow conditions. The erosion threshold and erosion rate are studied through step by step increasing the flow rate during a test. Results clearly indicate time-decreasing erosion during which individual flocs are randomly eroded, and time-independent (steady) erosion during which both sand and mud particles are continuously and uniformly eroded. These two erosion types appear to be floc and surface erosion, respectively (Winterwerp and Van Kesteren, 2004). Floc erosion relates to the stochastic character of both the flow conditions and (surficial) sediment strength, whereas surface erosion relates to the plasticity index, which is a bulk soil mechanical parameter characterizing cohesiveness. The surface erosion threshold is discussed following a geotechnical approach, which argues that surface erosion is a drained process. This implies that cohesiveness rather than packing density is important for the erosion threshold, which is confirmed by the experimental data. Simultaneously with the erosion tests, also the undrained shear strength of the applied soil samples was determined. A model is proposed and validated to predict the undrained shear strength as function of the granular porosity in combination with the plasticity index. The comparison of the undrained shear strength with the surface erosion threshold further confirms the applicability of a geotechnical approach to understand the erosion of mixed sediments. Finally, the study provides a valuable data set that can be used as a reference for future research on erosion behavior of (natural) sediment mixtures.

1. Introduction

Ecosystems in estuaries and tidal lagoons belong to the most valuable in the world. Managing authorities are therefore under strong pressure to compensate for human interferences in these systems. Morphological processes in estuaries and tidal lagoons are characterized by complex interactions between hydrodynamical, morphological and biological processes. This indicates that it is difficult to derive general applicable, process-based algorithms for morphological processes (e.g. erosion), which are important to predict consequences of, e.g. engineering works in marine wetlands.

The current study concerns the stability of muddy sediment beds as encountered in the marine environment. Although muddy sediments often concern mixtures of sand and mud, these fractions are often treated separately. Therefore, Van Ledden et al. (2004) propose a classification framework, as well as a heuristic formulation for the erosion behavior of sand–mud mixtures. However, both the framework and formulation lack proper experimental foundation.

The well-known Ariathurai–Partheniades formulation (Partheniades, 1962; Ariathurai, 1974) is applied for the heuristic formulation mentioned above:

$$E = M(\tau_b/\tau_e - 1) \qquad (1)$$

where E (kg m^{-2} s^{-1}) is the erosion rate, M (kg m^{-2} s^{-1}) an empirical erosion parameter, τ_b (Pa) the bed shear stress and τ_e (Pa) the erosion threshold. M and τ_e typically exhibits strong variations for both natural and artificially generated sediments, which are attributed to numerous biological (e.g. Le Hir et al., 2007b), chemical (Kandiah, 1974) and physical influences (Winterwerp and Van Kesteren, 2004) on the stability of intertidal sediments.

Current study focuses on the effect of physical influences on the erosion threshold of artificially generated sand–mud mixtures. Righetti and Lucarelli (2007) give an overview of previous

* Corresponding author. Tel.: +31 6 23034916.
E-mail addresses: w.jacobs@boskalis.nl, walterjacobs@hotmail.com, w.jacobs@tudelft.nl (W. Jacobs), plehir@ifremer.fr (P. Le Hir), Walther.vanKesteren@deltares.nl (W. Van Kesteren), Philippe.Cann@ifremer.fr (P. Cann).

studies on the erodibility of sediment mixtures. Most studies (e.g. Partheniades, 1962) relate τ_e to packing density and/or particle size only, whereas few studies acknowledge the importance of internal structure, cohesiveness, stress history and biological activity. Panagiotopoulos et al. (1997) relate transitions in erosion behavior to variations of the internal structure, as the internal friction angle of sediments with mud contents larger than 30% is significantly lower than for granular sediments. Torfs (1995) defines a 'transitional regime' for clay contents of 7–13%.

The only study relating τ_e to the cohesiveness of the sediment bed rather than to the clay content concerns Smerdon and Beasley (1959):

$$\tau_e = 0.163 PI^{0.84} \tag{2}$$

where cohesiveness is expressed by the plasticity index PI (%). However, the packing density is not incorporated in this formulation. In conclusion, only highly empirical formulations describing the erosion behavior of sand–mud mixtures rather than process-based formulations are available, which is attributed to a lack of insight into the determining processes for erosion of a sediment bed.

To obtain a more physically founded and, subsequently, a more general applicable erosion formulation, a more soil mechanical approach is required. Schofield and Wroth (1968) proposed the generally applied critical state model, which relates the mechanical behavior of soils to the applied loading conditions, on one hand, and the packing density, cohesiveness, stress history and permeability, on the other hand. Different types of soil mechanical yielding are defined.

Based on the geotechnical approach of Schofield and Wroth (1968), Winterwerp and Van Kesteren (2004) formulated four erosion modes: entrainment, floc erosion, surface erosion and mass erosion. Entrainment occurs when fluid mud is entrained by a turbulent flow. Floc erosion is the disruption of individual flocs from the surface of the bed by flow-induced peak bed shear stresses. Surface erosion is a drained failure process (no pore water pressure gradients), which occurs when the mean bed shear stress is larger than the mean erosion threshold. As a result, sand and mud simultaneously and continuously erode from the whole surface layer of the sediment bed, which is in contrast with the random (in both space and time) character of floc erosion. Finally, mass erosion is an undrained process during which lumps of material are eroded due to external fluid stresses, which largely exceed the cohesive bed strength as well as the strength resulting from pore water pressure gradients.

When the time scale of the forcing condition is relatively large compared to the flow-induced deformations of the sediment bed, pore water pressures are generated resulting in pore water flow following Darcy. When these time scales are similar, no pore water pressure gradients occur and the strength is referred to as the drained strength in geotechnical engineering. This drained strength is often referred to as the 'true' cohesive strength (Winterwerp and Van Kesteren, 2004). The undrained shear strength is also referred to as apparent cohesion. It is important to distinguish between these strengths as the undrained shear strength (100 kPa) generally largely exceeds the drained shear strength (< 10 Pa).

Winterwerp and Van Kesteren (2004) theoretically derive a formulation for surface erosion:

$$E = M_E(\tau_b - \tau_e)\rho_{dry}, \quad \text{where} \quad M_E = (c_v\phi_{s,0})/(10d_{50,f}c_u) \tag{3}$$

M_E (m Pa^{-1} s^{-1}) is an erosion parameter and ρ_{dry} (kg m^{-3}) the dry density of the bed. M_E is a function of the soil mechanical parameters c_u (Pa) and c_v (m^2 s^{-1}), which are the undrained shear strength and the coefficient of pore water dissipation, respectively. The sediment bed is characterized by the non-consolidated volume concentration ($\phi_{s,0}$ (−)) and particle size ($d_{50,f}$ (m)) of the

flocs, which are both determined by the cohesive and adhesive properties of mud. This formulation was compared to some experimental data and appeared promising, although a proper validation has not been executed yet.

A systematic research to quantify and qualify the newly proposed erosion formula is being executed. A first step concerned the individual study of the material parameters c_u and c_v as function of varying clay mineralogy and sand and mud content (Jacobs et al., 2007a,b). The current study is the second step. The objective is to study the surface erosion threshold by carrying out a large number of erosion tests on artificially generated sand–mud mixtures with varying clay mineralogy and structure. The third (future study) step concerns the erosion rate.

2. Theory

Sediment mixtures are not solely characterized by their density and/or clay content, as discussed in Section 1. Therefore, we discuss a parameter that incorporates three different soil classifications. The first concerns a commonly used classification based on the size distribution of the mass contents by dry weight and distinguishes the sand (ξ_{sa} (%), 63–200 μm), silt (ξ_{si} (%), 2–63 μm) and clay content (ξ_{cl} (%), < 2 μm). The mud content (ξ_{mu} (%)) is the sum of ξ_{cl} and ξ_{si}.

The second classification is based on the structure of a sediment bed. Fig. 1 shows three different regions divided by the minimum ($n_{sasi,min}$ (%)) and maximum granular porosity ($n_{sasi,max}$ (%)) of a sand–silt mixture. The granular porosity indicates the voids between sand and silt particles and is, therefore, plotted as function of the volume fraction of sand (ψ_{sa} (%)) in relation to the volume fraction of silt (ψ_{si} (%)):

$$\psi_{sa} = 100 - \psi_{si} = \phi_{sa}/(\phi_{sa} + \phi_{si}) \tag{4}$$

where ϕ_i is the volume concentration of fraction i. It is important to note that the granular porosity is not the same as the overall porosity. The first refers to the space between sand and silt particles only, whereas the second refers to the space between all particles (in the current study: sand, silt and clay particles). Therefore, the granular porosity yields the sum of the overall porosity and the space occupied by clay particles:

$$n_{sasi} = n + \psi_{cl}(100 - n) \tag{5}$$

where n (%) is the overall porosity and ψ_{cl} (%) the volume fraction of clay relative to the total volume of solids (ψ_{cl} is equal to ξ_{cl}
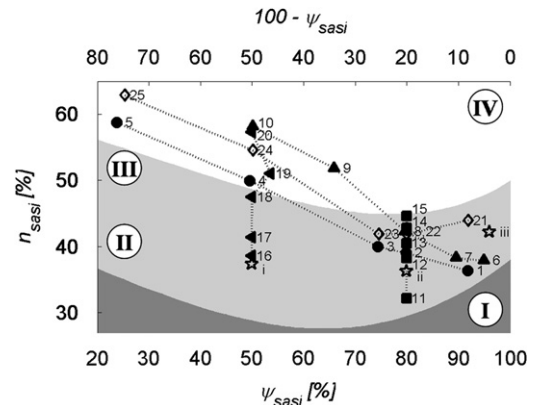

Fig. 1. Granular porosity as function of the sand (ψ_{sa})–silt (ψ_{si}) volume fraction ratio for sets 1 (●), 2 (▲), 3 (■), 4 (◄) and 5 (◇); the numbers refer to the sample numbers as shown in Table 1. For each set a transition in structures exists: from a sand–silt skeleton (light-grey area) to a clay–water matrix (white area). The roman numbers refer to Fig. 2. Due to the constant ratio between ξ_{si} and ξ_{cl}, an increase of ψ_{si} implies an increase of ξ_{cl}.
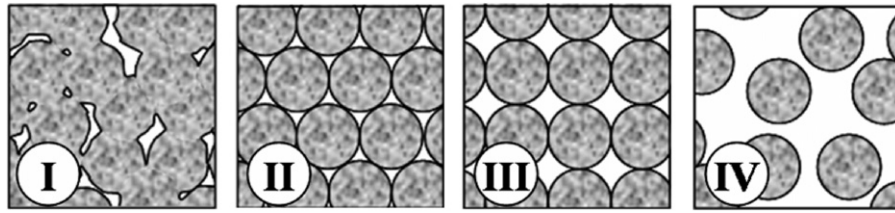
Fig. 2. Schematized packing densities of the granular (sand and silt) fraction. Below the minimum granular porosity ('I') particles are crushed, as in sedimentary rock. When sand and/or silt grains are in mutual contact, a densely ('II') or a loosely ('III') packed skeleton can occur. Quicksand or a clay–water matrix occurs when these grains are not in contact ('IV'). The Roman numbers refer to Fig. 1.

when the specific densities of all fractions are equal). The granular porosities are experimentally determined for different relations of sand and silt following ASTM D4254 (2006).

Fig. 2 illustrates four typical packing densities for sand and silt particles. For $n_{sasi} < n_{sasi,min}$ ('I') particles are crushed, which typically occurs for sedimentary rock. For $n_{sasi,min} < n_{sasi} < n_{sasi,max}$ sand and silt particles are in mutual contact and form a relatively stiff granular skeleton due to constrained particle movement. This skeleton can either be densely ('II') or loosely packed ('III'). For $n_{sasi} > n_{sasi,max}$ ('IV') particles are not in mutual contact as the granular porosity exceeds the porosity for which a skeleton occurs. This typically occurs for quick sand. For $n_{sasi} > n_{sasi,max}$, and when not only water but also clay particles are present, a clay–water matrix may exists. Sand and silt particles are kept in suspension for a sufficiently large cohesive strength of this matrix.

In the current study we apply mixtures of sand and mud, for which either a dominant clay–water matrix ($n_{sasi} > n_{sasi,max}$) or a non-cohesive granular skeleton ($n_{sasi,min} < n_{sasi} < n_{sasi,max}$) occurs. Herein, cohesion refers to the mutual bonding between clay particles; whereas adhesion (e.g. due to biogenic mucus) is not considered. Furthermore, Fig. 1 shows that when considering cohesive behavior to occur for $n_{sasi} > n_{sasi,max}$, the clay content is not the only discriminator of the offset for cohesive behavior, as $n_{sasi,max}$ varies for varying sand–silt ratios.

The third classification concerns the Atterberg limits (Skempton, 1965), which are commonly applied in geotechnical engineering, as numerous empirical relationships have been found between these limits and soil mechanical behavior (e.g. permeability and strength). These limits refer to different levels of consistency and characterize the capacity of clay to bind water. Fig. 3 shows that the plasticity index (PI (%)) yields the water content for which a soil exhibits plastic behavior. The water content is defined as the mass of water divided by the mass of dry sediment (multiplied by 100 when expressed in %). PI is a measure for cohesiveness and equals the difference in water content between the liquid (LL (%), transition from liquid to plastic behavior) and plastic limit (PL (%), transition from plastic to solid behavior). PI is shown to vary linearly with the clay content (Skempton, 1965):

$$PI = LL - PL = A(\xi_{cl} - \xi_{cl,0}) \qquad (6)$$

where A (–) is the activity of a soil and $\xi_{cl,0}$ (%) the onset clay content for cohesive behavior ($PI > 0$). The activity depends on the clay mineralogy and may vary considerably (0–10). Empirical geotechnical studies (e.g. Head, 1980; ASTM D2487, 2006) identify the transition from granular to plastic behavior to $PI \approx 7$.

In the current study, A is determined (following ASTM D4318, 2000) for the cohesive soils only, as the plasticity of the granular soils is too low to determine experimentally. Therefore, PI is indirectly determined by multiplying ξ_{cl} and A. The indirect plasticity index is expressed as PI^* (%), and enables the comparison of the 'cohesiveness' of both granular and cohesive soils.
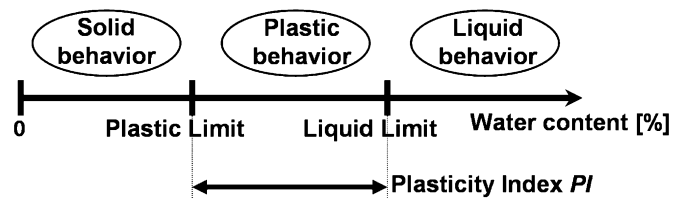

Fig. 3. Schematic depiction of the Atterberg limits, showing the plastic (PL) and liquid limit (LL). The limits reflect water contents for which the behavior of a soil changes from solid to plastic and from plastic to liquid, respectively. The difference between these water contents is the plasticity index (PI).

Next, we introduce the relative water content (W_{rel} (–)), which combines the three aforementioned classifications:

$$W_{rel} = W/PI^* \qquad (7)$$

where W (%) is the water content. It should be noted that W can be larger than 100%. W_{rel} is a useful discriminator parameter to compare sediment behavior of soil samples with varying compositions, degrees of cohesiveness and/or structures. It is noted that decreasing ξ_{cl} generates increasing W_{rel}.

3. Methods

Reproducible, homogeneously mixed and 100% saturated (with water) sand–silt–clay mixtures were artificially generated using a specific experimental procedure (Jacobs et al., 2007a). Sand, silt and clay fractions were oven-dried to disaggregate the material and, subsequently, manually mixed and placed in cylindrical containers (diameter=9 cm, height=10 cm). Pouring water on top of dry mixtures would cause blocking of small pores by the surface tension of water, which generates partly saturated samples. Therefore, the containers are placed in an exsiccator first to remove air. Next, the exsiccator (low pressure) is filled with CO_2 from a pressurized tank (using the difference with the atmospheric pressure), after which the pressure in the exsiccator is lowered again to replace enclosed air with CO_2.

Subsequently, mixtures are left for 24 h in the exsiccator, in which a layer of water was present. The combination of the low pressure (reduced surface tension), 100% humidity and the attractive forces of the negatively charged clay particles enables water molecules to 'activate' the clay fraction. The second part of the saturation process concerns the placement of a layer of 10 cm de-aired and demineralised water on top of the samples. Using the difference between the atmospheric and the reduced pressure within the exsiccator, water percolated through the mixture thereby completing the saturation procedure. To minimize anisotropic effects, erosion tests were executed quickly after generation of the samples.

Sediment compositions were chosen such that the effect of a transition in dominant structure (sand–silt skeleton or clay–water matrix) on erosion could be studied. This resulted in relatively densely packed soils, as for n_{sasi} close to $n_{sasi,max}$ (≈ 0.45) and

$\xi_{cl} \approx \psi_{cl} \approx 10\%$ the bulk density $\rho_{bulk} \approx 1800\text{–}2000$ kg m^{-3}. Four different sets of soil samples with increasing ξ_{cl} and varying clay–silt ratio (sets 1 and 2) and sand–silt ratio (sets 3 and 4) were tested (Table 1). Natural sediments in marine systems typically exhibit constant clay–silt ratios (Flemming, 2000).

Additionally, two different clay minerals were applied: kaolinite for sets 1–4 and bentonite (montmorillonite type of clay) for set 5, which exhibited a similar granular composition as set 1. Soil samples of set 0 (i, ii and iii) consisted of sand and silt only, with n_{sasi} just above $n_{sasi,min}$. These set 0 compositions are located on the lower ends of the dotted lines in Fig. 1 (indicated by the stars). Their sand–silt ratios relate to set 4 (no. i), set 3 (no. ii) and sets 1, 2 and 5 (no. iii).

The grain size distribution of the individual fractions was determined using a Sedigraph. These analyses, as well as the Atterberg limits and the determination of $n_{sasi,min}$ and $n_{sasi,max}$, were executed at a geotechnical institute (Deltares, the Netherlands). W was determined by oven drying at 105 °C for 24 h. The median particle diameter (d_{50} (m)) of the sand fraction was 170 μm, and for silt $d_{50} = 28$ μm. The activity (see Eq. (6)) of kaolinite and bentonite was 0.67 and 1.34, respectively (following from experimental determination of the Atterberg limits). Sedigraph tests show that the utilized kaolinite and bentonite exhibit 31% and 54% clay fraction, respectively, which implies that a considerable amount of this material consists of silt. It should be noted that the application of other methods (e.g. Coulter Counter, Malvern) to determine the clay content of the same material resulted in variations for ξ_{cl} up to 100% (Jacobs et al., 2007a).

All sediment samples were generated twice; one was applied for two erosion tests, the other to determine the undrained shear strength. The strength was determined according ASTM D4648 (2005), using an Anton Paar Physica MCR 301 rheometer with a 6-bladed vane with a width of 2.2 cm and a height of 1.6 cm. The vane was rotated at constant rate (1 rpm) for ten revolutions.

The measured average residual torque (as function of the rotation angle) was converted to the undrained shear strength.

Erosion tests were executed using the small-scale (1.20 m long, 8 cm wide and 2 cm high) straight transparent flume (Erodimetre, Le Hir et al., 2006, 2007a; Fig. 4(a)) at the French research institute Ifremer in Brest. Sub samples with a thickness of 2–3 cm were obtained from the mother sample with a cutter. These slices were slipped into a cylindrical container with identical diameter, which was fixed to the flume (Fig. 4(b)). Next, the surface of the soil sample was horizontally and vertically leveled with the bottom of the flume. The whole exposed surface area was presumed to contribute to erosion. The bottom of the flume was covered with sandpaper (with a roughness comparable to the applied sand fraction) to reduce differences in roughness with the sample. In practice, nearly no scour was observed at the upstream boundary of the samples. A unidirectional flow generated by a re-circulating pump was accelerated step by step (average duration of a step approximately 150–200 s), until a layer of a few mm was eroded. A flow meter in the pump
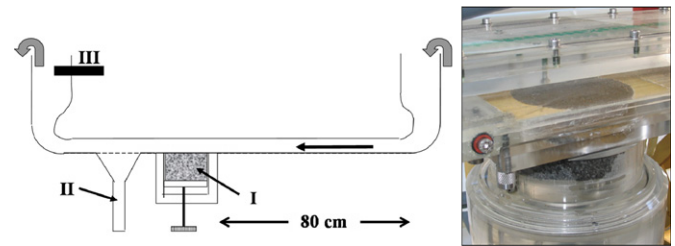
Fig. 4. Re-circulating flume 'Erodimetre' as applied in the current study (after le Hir et al., 2006, 2007a). The left panel shows a schematic depiction of the flume with the flow direction indicated by the black and grey (block) arrows, and a soil sample by the hatched area (I). Downstream a sand trap (II) and turbidity meter (III) are mounted. The right panel shows detail of the flume with a soil sample.

Table 1

Composition and bulk properties of the tested soils. For sets 1, 2 and 5 the clay–silt ratios are constant: 0.25, 0.4 and 0.25, respectively; for sets 3 and 4 the sand–silt ratio is constant: 0.8 and 0.5, respectively (see values in italic). The applied clay mineral for sets 1–4 is kaolinite and for set 5 bentonite. All soil samples are tested twice, which is reflected by two values for ρ_{bulk}, W, n_{sasi} and W_{rel}. The bold numbers refer to soil samples exhibiting feature 2.

	No.	ξ_{cl} (%)	ξ_{si} (%)	ξ_{sa} (%)	ξ_{cl}/ξ_{si} (−)	ψ_{sasi} (%)	ρ_{bulk} (kg m^{-3})		W (%)		n_{sasi} (%)		PI* (%)	W_{rel} (−)	
Set 0	i	2	49	49	0.05	50	2028	2040	21	21	37	37	0	–	–
	ii	1	20	79	0.05	80	2029	–	21	–	36	–	0	–	–
	iii	0	4	96	0.04	96	1948	–	27	–	41	–	0	–	–
Set 1	1	2	8	90	0.25	92	2039	2017	21	22	36	38	1.3	15.5	16.4
	2	5	19	76	0.25	80	2024	2077	22	19	39	36	3.2	6.7	5.8
	3	6	24	70	0.25	74	2021	2046	22	20	40	39	4	5.4	5.1
	4	11	45	44	0.25	50	1901	1947	30	27	50	47	7.5	4	3.5
	5	16	64	20	0.25	24	1784	1804	40	38	59	58	10.7	3.7	3.6
Set 2	6	2	5	93	0.40	95	2014	–	22	–	38	–	1.3	16.6	–
	7	4	10	86	0.40	90	–	2028	–	21	–	38	2.7	–	8
	8	7	19	74	0.40	80	1998	2020	23	22	42	41	5	4.6	4.4
	9	12	30	58	0.40	66	1875	1920	32	28	52	49	8	4	3.5
	10	17	42	42	0.40	50	–	1802	–	38	–	58	11.1	–	3.4
Set 3	11	3	19	78	0.15	80	–	2120	–	17	–	32	2	–	8.2
	12	5	19	76	0.25	80	2038	2079	21	19	38	36	3.2	6.5	5.8
	13	6	19	75	0.32	80	2013	2022	22	22	40	40	4	5.5	5.4
	14	7	18	74	0.40	80	1989	2002	24	23	43	42	5	4.8	4.6
	15	8	18	74	0.44	80	1964	2005	25	23	45	42	5.4	4.7	4.2
Set 4	16	2	49	49	0.05	50	2007	2091	23	18	39	33	1.6	14.1	11.2
	17	5	47	47	0.12	50	1992	2017	24	22	41	40	3.7	6.4	6
	18	8	46	46	0.19	50	1918	1931	29	28	47	47	5.7	5	4.9
	19	12	41	47	0.29	54	1887	1872	31	32	51	52	7.8	3.9	4.1
	20	16	42	42	0.39	50	1819	1816	37	37	57	57	11	3.3	3.3
Set 5	21.	2	8	90	0.25	92	–	1915	–	29	–	44	1.3	–	22.1
	22	5	19	76	0.25	80	1976	–	25	–	42	–	5	4.9	–
	23	6	24	70	0.25	75	1989	1997	24	23	42	41	6.6	3.6	3.5
	24	11	44	45	0.25	50	1817	–	37	–	55	–	13.5	2.7	–
	25	16	63	21	0.25	25	–	1704	–	49	–	63	19.7	–	2.5

controlled the flow rate. The short duration of a test (2 h, including installation and cleaning), enabled the execution of a large number of tests.

The erosion behavior of coarse particles was derived from a transparent sand trap downstream of the sediment sample by recording the volume of sand (by means of visual observations) at the end of each discharge step. After a test, the total mass of sand was proportionally divided over the steps. The grain size distributions of both the original soil samples and the sand trap material were determined using a laser-granulometer. The suspended sediment concentration was derived from continuous data obtained by an optical backscatter turbidity meter (*Seapoint*). This meter was calibrated from water samples, which were divided in three groups based on the dominant type of sediment in the fines fraction ($<63\,\mu m$): silt (soil samples i, ii, iii, 1, 6, 7 and 21), silt and kaolinite (2–5 and 8–20) or silt and bentonite (22–25). For each group a different calibration curve related the output of the turbidity meter (T (V)) to the concentration of suspended sediments c ($g\,l^{-1}$): $c=289T$ for silt, $c=157T$ for kaolinite and $c=258T$ for bentonite.

The calibration of the bed shear stress is not straightforward, as the bed roughness is likely to vary in space and even in time during the erosion process. However, a turbulent flow in the flume can be assumed, except for very low discharges in the flume. Then the bed shear stress is assumed proportional to the square of discharge in the flume. The drag coefficient has been fitted so that the initiation of movement of monodisperse sand (test iii) is consistent with the critical mobility parameter given by the Shields diagram.

Of course, the calibration of τ_b is an estimation, for example due to the high sensitivity of the drag coefficient for small variations of the Reynolds number especially when discharges are low. Furthermore, additional friction generated along the upper side of the test section is not taken into account in the assumption of the closed conduit flow. In conclusion, the presented calibration of τ_b enables the discussion of relative variations of the critical bed shear stress for erosion, although care should be taken when discussing absolute values and/or when comparing results with other studies.

4. Results

4.1. Erosion modes and features

Based on the erosion classification as discussed in Section 1, and the characteristics of the tested soil samples both floc and surface erosion are expected to occur during the tests. Observations during the erosion tests confirm that already for low τ_b individual flocs randomly erode from the sediment bed. For increasing τ_b, a certain threshold occurs for all soil samples, above which sand and mud particles uniformly erode from the exposed surface area. Uniform erosion is illustrated by the smooth surface indicated in Fig. 5(a). Fines are transported as suspended load after erosion, whereas sand and aggregates are transported as bed load and deposit in the sand trap within seconds after erosion. Identical behaviors exist for soil samples with kaolinite and bentonite.

However, also two features are observed above the surface layer of some soil samples (Table 2), simultaneously with the occurrence of surface erosion. The first is a transport feature and concerns the development of a sand wave for sandy soil samples ($\xi_{sa}>90\%$) after the initiation of motion. This sand wave travels along the bottom of the flume towards the sand trap, thereby
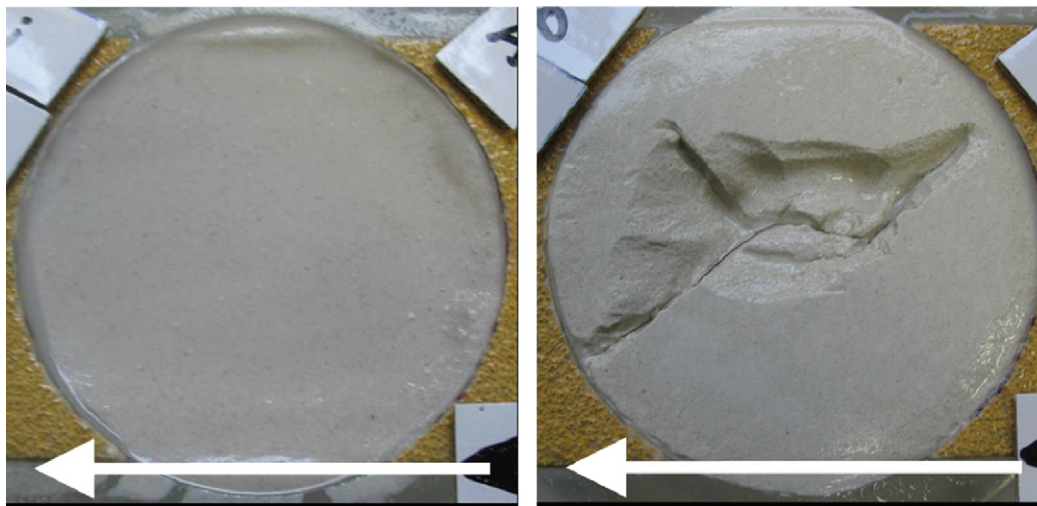

Fig. 5. The panel at left shows a smooth surface after surface erosion for soil sample 16 ($\xi_{cl}=2\%$, $\xi_{si}=49\%$, $\xi_{sa}=49\%$), which exhibits a dominant sand–silt skeleton. The panel at right shows a typical example of feature 2 for sample 20 ($\xi_{cl}=16\%$, $\xi_{si}=42\%$, $\xi_{cl}=42\%$), which exhibits a dominant clay–water matrix. The flow direction is indicated by the white horizontal arrow.

Table 2
Overview of features observed during surface erosion, in relation to the accompanying soil samples characteristics. The numbers in the second row refer to the sample compositions indicated in Table 1.

	Feature 1	No feature	Feature 2
Sample no.	iii, 1, 6, 7, 21	i, ii, 2, 3, 8, 11–19, 22–24	4, 5, 9, 10, 20, 25
Dominant structure	Sand–silt skeleton	Sand–silt skeleton	Clay–water matrix
Mud content	$\xi_{mu}<10\%$, $\xi_{sa}>90\%$	$10\%<\xi_{mu}<56\%$	$42\%<\xi_{mu}<80\%$
Erosion mode	Floc, surface	Floc, surface	Floc, surface, lump
Bed load (sand)	Sand wave migration	Individual particles	Individual particles
Transport of mud	Suspended load	Suspended load	Suspended load+aggregates

generating a time lag in the order of minutes between erosion and deposition in the sand trap.

The second feature concerns uneven erosion patterns caused by the development of cracks within the surface of soil samples, which exhibit a dominant clay–water matrix (Fig. 5(b)). These either radial (mostly) or longitudinal cracks (parallel to the flow direction) expand with increase in τ_b. Before and during the formation of these cracks, individual flocs and sand grains are simultaneously eroded. However, also aggregates of sediment are randomly eroded from the cracks, which explain the uneven erosion pattern. The erosion of aggregates is confirmed by grain size analyses of the sand trap material, which indicate significant ξ_{mu} for soil samples exhibiting feature 2 (normally almost no mud is found in the sand trap after an erosion test). Table 2 shows that the transition between uniform surface erosion and the occurrence of feature 2 occurs for $n_{sasi} \approx n_{sasi,max}$ for all sets. Only for set 3 feature 2 did not occur, as n_{sasi} for all samples of this set was smaller than $n_{sasi,max}$.

4.2. Erosion threshold

Typical results of a test are shown in Fig. 6. The erosion flux for fine material (E_{mud} (kg m^{-2} s^{-1})) is determined by dividing the time derivative of the continuously recorded turbidity by the surface area of the samples (~ 60 cm^2). The erosion flux of the coarse material (E_{sand} (kg m^{-2} s^{-1})) is derived in a similar way. However, these fluxes are considered less accurate as the amount of eroded coarse material was not continuously recorded.
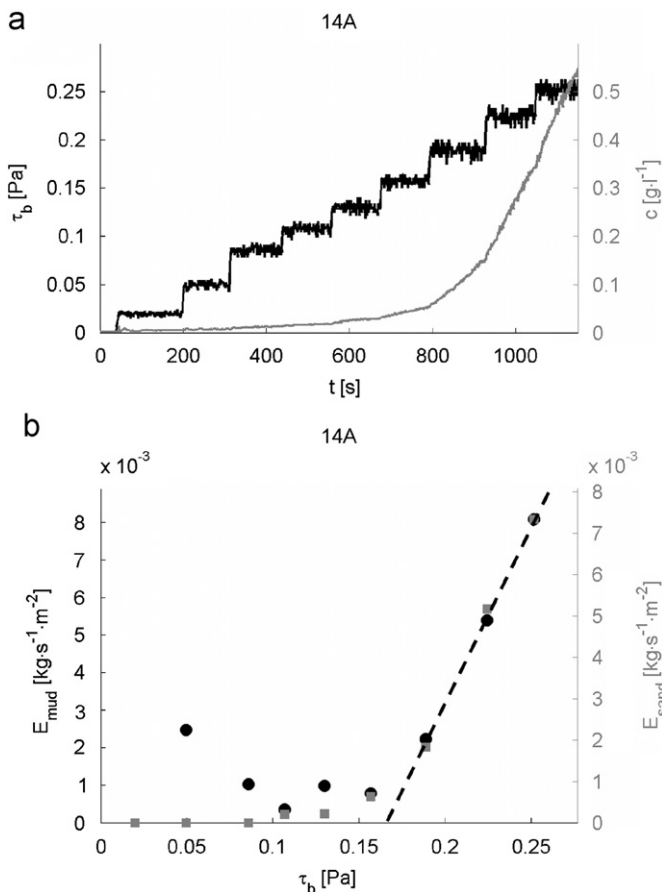

Fig. 6. Typical results of erosion test on sample 14 ($\xi_{cl}=7\%$, $\xi_{si}=18\%$, $\xi_{cl}=75\%$) showing in black the step-by-step increased τ_b (a, left vertical axis) and in grey the concentration (right vertical axis) as function of time (t (s)), and in (b) the erosion fluxes of mud (left vertical axis, black circles) and sand (right vertical axis, grey squares) as function of τ_b. The averaged extrapolated zero erosion rates determine the erosion threshold for surface erosion.

Fig. 6(a) shows that the initially (low τ_b) observed erosion exhibits a time-decreasing behavior, with a relatively sharp increase of c at the start of a new τ_b-step followed by an equilibrium condition (constant c). Fig. 6(b) shows that this behavior results in initially large E_{mud}, and that during this time decreasing and limited supply process only mud is eroded. Furthermore, no clear erosion threshold, but a range of τ_b exists for which flocs are continuously eroded. Similar behaviors are observed for soil samples containing only silt, kaolinite and silt or bentonite and silt.

For larger τ_b, time independent and unlimited supply erosion occurs, which is characterized by a linear increase of c with time (Fig. 6(a)). Furthermore, Fig. 6(b) shows that a clear threshold τ_b can be identified, above which sand and mud particles are simultaneously eroded, uniformly from the whole exposed surface area. This threshold concerns the onset of transport, rather than a threshold for the initiation of motion. Time-decreasing and time-independent erosion agree with floc and surface erosion, respectively. This is further discussed in Section 5. Current study focuses on the surface erosion threshold. According to the quasi-linear relationship between E and τ_b (see e.g. Fig. 6(b)), the threshold is selected as the average abscissa of the extrapolated E_{sand} and E_{mud}, assuming the linear relationship remains valid.

Fig. 7 shows τ_e for all soils listed in Table 1 as function of W, which represents the packing density. Generally, it is presumed that τ_e decreases for a looser packing density, and therefore, for increasing W. However, Fig. 7 clearly shows a contradicting behavior, as τ_e becomes larger for increasing W. Finally, Fig. 7 indicates that τ_e ($< \sim 0.5$ Pa) for sand–mud mixtures with low ξ_{cl} and low W ($< 25\%$, see the black squares, triangles and circles), tend to τ_e for mixtures of sand and silt only (see stars).

Next, τ_e is plotted as function of PI^* in Fig. 8. The erosion threshold exhibits a clear power law relation with the plasticity index for $PI^* > 2$:

$$\tau_e = 0.161 PI^{*0.80} \tag{8}$$

Although $PI^* \approx 5$–7 indicates the onset for cohesive behavior, Eq. (8) applies to the behavior of τ_e for both a dominant sand–silt skeleton and a clay–water matrix. For $PI^* < 2$, τ_e tends to τ_e for mixtures of sand and silt, for which τ_e increases with increase in ξ_{si}. However, these granular mixtures ($PI^*=0$) exhibit larger τ_e compared to soils for which $PI^* > 0$.

τ_e for low cohesive soils ($PI^* < 2$) is plotted in Fig. 9 as function of ψ_{sasi}. It is shown that τ_e increases for increasing silt content, and that τ_e for soil samples of sets 1–5 with little clay, similar τ_e exist as for set 0 soils. The figure indicates a linear relation between
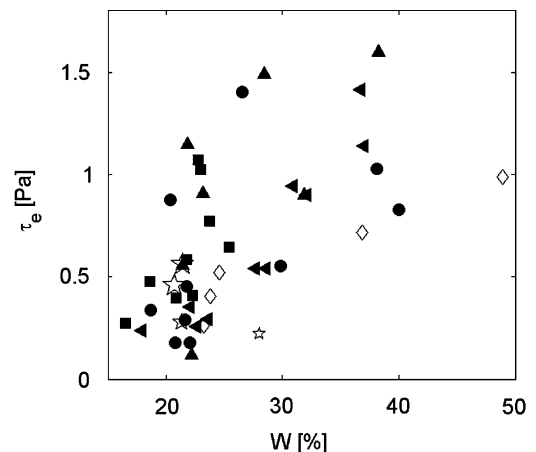

Fig. 7. Surface erosion threshold as function of the water content for soil samples of sets 0 (∗), 1 (●), 2 (▲), 3 (■), 4 (◀) and 5 (◇). The size of the markers of set 0 increases with increase in silt content.
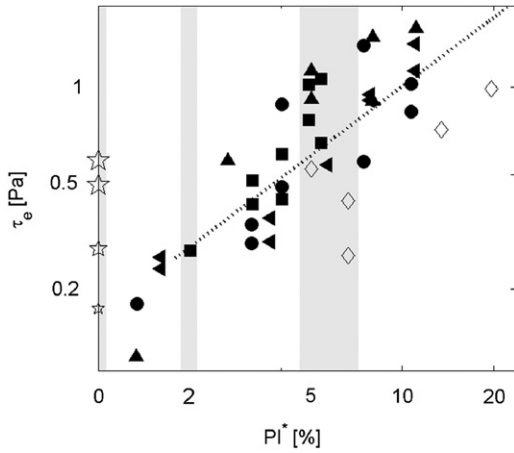
Fig. 8. Surface erosion threshold as function of the plasticity index (PI^*) for sets 0 (✳), 1 (●), 2 (▲), 3 (■), 4 (◄) and 5 (◇). The size of the markers of set 0 increases with increased in silt content. The grey-hatched areas indicate $PI* = 0$, $PI^* \approx 2$ and $PI^* \approx 5–7$, which refer to non-cohesive soils, the offset for cohesive effects and the transition between a sand–silt skeleton and clay–water matrix, respectively.
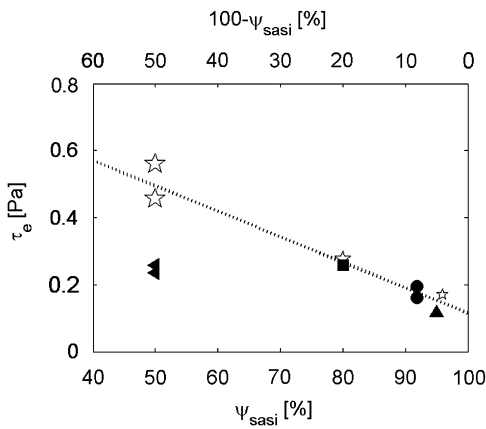

Fig. 9. Surface erosion threshold as function of the ratio between sand and silt volume fraction for sets 0 (✳), 1 (●), 2 (▲), 3 (■) and 4 (◄) for which the plasticity index is < 2. The dotted line is the fit for all data, except of set 4.

ψ_{sasi} and τ_e for soil samples i, ii, iii, 1, 6 and 11. τ_e for soil sample 16 deviates from this linear relation.

4.3. Undrained shear strength

For the compositions shown in Table 1 c_u is measured; only for samples of set 0 the test could not be executed because the packing density was too high to insert the vane. Results are shown in Fig. 10. Although the data are slightly scattered, two modes are clearly distinguished. When adding clay (i.e. decreasing W_{rel}) to a mixture of sand and silt, c_u first decreases for a dominant sand–silt skeleton (right branch in Fig. 10) and, subsequently, increases for a dominant clay–water matrix (left branch).

5. Discussion

5.1. Erosion modes

The erosion of aggregates and the occurrence of cracks associated with feature 2 would suggest mass erosion. However, the magnitude of τ_b during the tests (maximum ~ 3 Pa) is too low to generate the undrained process of mass erosion, as the mass
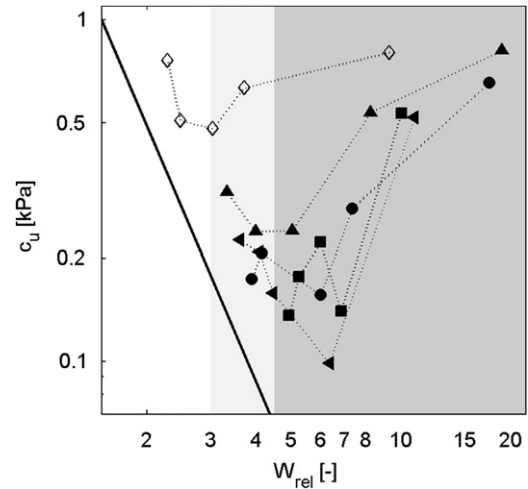

Fig. 10. Undrained shear strength (c_u) as function of the relative water content ($W_{rel} = W/PI^*$) for sets 1 (●), 2 (▲), 3 (■), 4 (◄) and 5 (◇) as shown in Table 1. The data show a transition in behavior for increasing W_{rel}. For increase in small W_{rel}, c_u decreases and for larger increase in W_{rel}, c_u increases. Note that the clay content increases towards the left. The continuous line indicates the strength of mixtures of water and clay as reflected by Eq. (9). The dark-grey and light-grey hatched areas indicate the areas for which soils with kaolinite and bentonite, respectively, exhibit a sand–silt skeleton.
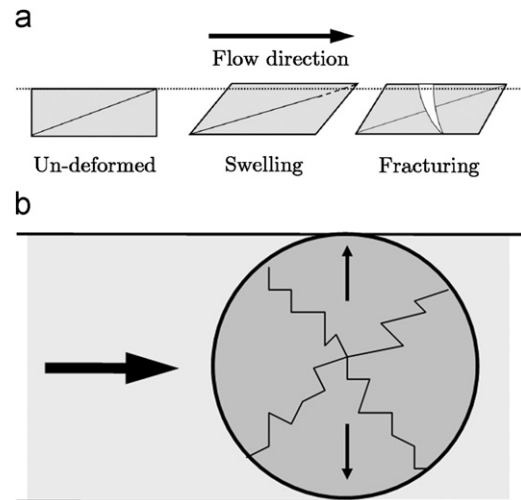

Fig. 11. Failure mechanism of mass erosion ((a) side view), with failure planes perpendicular to the flow direction (after Van Kesteren, in preparation), and failure mechanism as observed in the current study ((b) top view) for radial failure planes. The large black arrows indicate the flow direction.

erosion threshold typically equals $2–5 \cdot c_u$ (Winterwerp and Van Kesteren, 2004) and the c_u-value of the tested soil samples is ~ 1 kPa. Besides, the observed behavior does not agree with the failure mechanism of mass erosion (Fig. 11(a)). This mechanism exhibits flow-induced deformations in plastic material, which generate swelling in the flow direction and, subsequently, cracks perpendicular to the flow direction. The characteristics of these cracks are markedly different from the longitudinal and radial cracks observed for feature 2.

Although feature 2 clearly illustrates differences in behavior between granular and cohesive soils, the longitudinal and radial cracks are most likely artifacts of the experimental set-up rather than indicators of mass erosion. Longitudinal cracks may be attributed to distortion resulting from a combination of the (small) margin between the soil sample and the bottom of

the flume, on the one hand, and the force exerted by the flow, on the other. Distortion is largest in the middle of the soil samples and almost zero along the sides due to the circular shape of the exposed area. Another effect of the margin between the soil sample and the flume may be that the exposed surface area becomes slightly oval-shaped (Fig. 11(b)). The upstream and downstream parts of the surface area act as a wedge and generate radial failure planes, which agrees with dilating shear planes for low isotropic stress (Winterwerp and Van Kesteren, 2004).

True mass erosion yields an undrained failure process during which lumps of material are eroded. However, based on the relatively low τ_b in relation to the relatively large c_u the erosion of the lumps of material as observed for feature 2 must be a drained process. This is explained by the presence of the cracks, which allow the dissipation of pore water pressure gradients at relatively large and random depth and, subsequently, the drained erosion of lumps of material.

This crack formation and the subsequent erosion of lumps of material can be compared with cliff erosion due to wave action as observed at the transition between tidal flats and marshes in estuaries. A dissipation front propagates horizontally into the cliff; erosion of lumps of material occurs when the flow-induced stresses (in combination with a gravitation component) exceed the drained strength of the cliff.

In conclusion, the longitudinal and radial cracks which characterize feature 2 are most likely artifacts of the experimental set-up. Furthermore, the cracks generate drained erosion of lumps of material that should not be confused with true mass erosion following Winterwerp and Van Kesteren (2004). Therefore, it is difficult to analyze this type of erosion quantitatively.

5.2. Time-decreasing and time-independent erosion

The determination of the erosion threshold is often subject of discussion, as there is no clear definition. This is primarily caused by the fact that for any given bed shear stress always some particles are moved and/or eroded, which results in a range of τ_e for the onset of time-decreasing erosion as shown in Fig. 6(a). However, Fig. 6(b) also shows that for time-independent erosion that occurs for larger τ_b, a clear threshold can be identified by extrapolating to a zero erosion rate. Observations during the erosion tests indicate that this threshold reflects the onset of uniform erosion of both sand and mud, whereas for time-decreasing erosion only flocs were randomly eroding.

Time-decreasing and time-independent erosion agree, respectively, with Types I and II erosion as defined by Parchure and Mehta (1985), see also Sanford (2006). However, they relate depth-limited (i.e. time-decreasing) erosion to increasing bed strength with increasing depth only. In the current study soil samples are isotropic concerning packing density and composition, which indicates that vertical gradients of the bed strength within the upper few mm are (presumably) too small to significantly decrease erodibility. Other possible causes for the occurrence of time-decreasing erosion in the current study are briefly discussed below.

The first possibility concerns the erosion depth; when it becomes too large it may affect the flow pattern and, therefore, the erosion behavior. However, the final erosion depth for most tests is only about 2 mm (10% of the water depth), which is presumed too small to affect erosion. Besides, upon the transition from time-decreasing to time-independent erosion the erosion depth is much less than 2 mm. The second possibility is that during time-decreasing erosion only flocs are eroded. The remaining sand–silt skeleton consists of larger particles, which are more difficult to erode (cf. armoring; e.g. Van Rijn, 1993). Also

the occurrence of simultaneous erosion and deposition of mud (especially for high concentrations) may result in a zero net water-bed exchange. However, time-decreasing erosion only occurs during the first velocity steps, whereas the effect of armoring and deposition are especially expected for relatively large τ_b and c.

The third possibility is that time-decreasing erosion originates from the stochastic characters of τ_b and τ_e. Also e.g. Vanoni (1964), Partheniades (1965), Grass (1970), Torfs (1995), Panagio-topoulos et al. (1997), Righetti and Lucarelli (2007) and Van Prooijen and Winterwerp (2010) relate the absence of a true erosion threshold for cohesive sediments to these stochastic characters. As the bed shear stress is the sum of a mean value ($\overline{\tau}_b$) and turbulent fluctuations ($\hat{\tau}_b$), the erosion of particles may start already for small τ_b when $\hat{\tau}_b$ exceeds the strength of the weakest flocs.

The above listed studies also observe a sudden increase of the size and quantity of flocs in the water column, as well as the start of the erosion of sand for larger τ_b ($\overline{\tau}_b > \tau_e$), which reflects Type II erosion. Partheniades (1965) further argues that the horizontal distribution of the bed strength (and thus τ_e) further enhances time-decreasing effects. However, in the current study it is presumed that this effect is small, as the exposed surface area is small and the soil samples are isotropic.

The stochastic approach agrees with the proposed erosion classification. Floc erosion is the disruption of individual flocs from the surface of the bed by flow-induced peak bed shear stresses when the mean bed shear stress not yet exceeds the mean bed drained strength. In time, the weakest particles erode. This forces the probability density function of the bed strength to shift to larger values and, as a result, floc erosion ceases. Surface erosion is a drained failure process (no pore water pressure gradients), which occurs when the maximum bed shear stress is larger than the maximum erosion threshold. As a result, the supply of sediments is unlimited yielding a constant erosion rate of sediments for the whole surface layer of the sediment bed. This is in contrast with the random (in both space and time) character of floc erosion. Current study focuses on the surface erosion threshold, which relates to soil characteristics (sediment strength) rather than to the stochastic character of the flow as is the case for time-decreasing or floc erosion.

5.3. Surface erosion threshold for sand–mud mixtures

Figs. 7 and 8 show that τ_e typically varies between 0.1 and 1.5 Pa, which agrees with reported data for low-cohesive soil samples (e.g. Le Hir et al., 2007b; Winterwerp and Van Kesteren, 2004). However, a negative correlation occurs for τ_e as function of W, which is explained by the water binding capacity of clay. Larger ξ_{cl} generates larger W (Table 1), which indicates that simultaneously with a decreasing packing density, ξ_{cl} and, subsequently, τ_e increase. Furthermore, Figs. 7 and 8 confirm the presumed drained character of surface erosion, as its thresh-old relates to PI^* (Fig. 8), which is measure of the cohesiveness (and, therefore, for the drained shear strength), rather than to packing density (W, Fig. 7). The scattering of the data in both figures may be attributed to the (unknown) effect of varying clay–silt and sand–silt ratios on PI^*.

Next, the experimental data are compared (Fig. 12) with the results of Smerdon and Beasley (1959) and Torfs (1995). Some assumptions are made concerning the composition of the applied soils by Torfs (1995), as only limited information is available. Soils are relatively sandy mixtures of sand and mud with a presumed dominant sand–silt skeleton and with assumed activities of 0.4 for kaolinite, 0.5 for natural clay (mainly illite) and 1.34 for
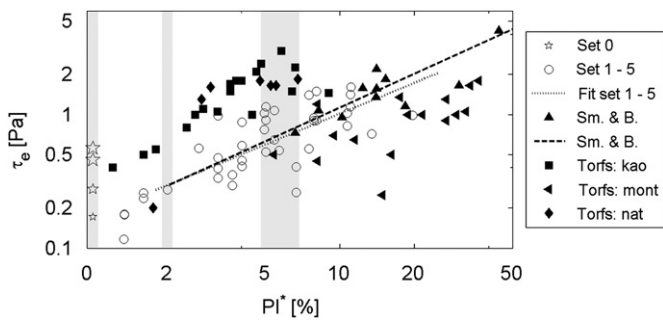
Fig. 12. Surface erosion threshold as function of the plasticity index (PI^*) for data of sets 0–5, Smerdon and Beasley (1959, Sm. & B.) and Torfs (1995). The grey-hatched areas indicate $PI^*=0$, $PI^* \approx 2$ and $PI^*=5–7$, which refer to PI^* of sand–silt mixtures, the offset for cohesive behavior and the transition between a dominant sand–silt skeleton ($PI^* < 5–7$) and clay–water matrix ($PI^* > 5–7$), respectively. The size of the markers of set 0 increases with increase in silt content.

bentonite. These agree with the activities of the clay minerals applied for the current study (kaolinite and montmorillonite) and with activities reported in literature (e.g. Head, 1980). Smerdon and Beasley (1959) study natural, riverine mud with an activity of the clay fraction of 0.9. As for these soils $PI^* > 7$, a dominant clay–water matrix is presumed for these soils.

Neither Smerdon and Beasley (1959) nor Torfs (1995) distinguish between floc and surface erosion. Torfs (1995) applies τ_e as τ_b for which material starts to accumulate in the sand trap in combination with a visually observed increase of the concentration of suspended fines. Smerdon and Beasley (1959) relate the erosion threshold to general movement of the soil composing the bed. This indicates that both studies define τ_e as τ_b for which transport is initiated, similar to the current study, which justifies the comparison of the results of the three studies.

Fig. 12 shows that the power law relation (Eq. (8)) between PI^* and τ_e for the experimental data nicely agrees with the relation presented by Smerdon and Beasley (1959). Re-plotting the results of Torfs (1995) also indicates a power law relation, although τ_e exhibits significantly larger τ_e (factors 2–4). A possibility for these larger τ_e may be the application of a different method to determine ξ_{cl}, which can result in differences for ξ_{cl} up to 100% (Jacobs et al., 2007a). An underestimation of the clay contents yields lower PI^*, which may explain the relatively large τ_e for given PI^*. The calculation of the bed shear stress may be another possibility. Torfs (1995) determines the bed shear stress based on the water surface slope, which is very inaccurate.

Summarizing, it is remarkable that for all three studies power law relations exists for τ_e as function of PI^*, although sediment mixtures with varying structures and clay mineralogy are applied. This confirms the applicability of the plasticity index rather than the packing density to relate to the surface erosion threshold, and also confirms the presumed drained character of surface erosion and the, subsequently, dominant effect of the cohesiveness of the clay fraction.

5.4. Erosion threshold for granular soil samples

The erosion threshold for granular mixtures ($PI^* < 2$) deviate from the power law function given by Eq. (8). Furthermore, it is not useful to relate τ_e to W, as the packing density for samples of set 0 exhibits only little variation (Table 1). Therefore, τ_e is plotted as function of ψ_{sa} in relation to ψ_{si} (Fig. 9). Results show that τ_e linearly increases for increasing silt content, and that soil samples of sets 1–5 with a low clay content (soil samples 1, 6, 11 and 16)

exhibit similar τ_e as found for set 0. The deviation of τ_e of soil sample 16 deviates from this linear relation, which is attributed to the relatively large ξ_{mu} (50% for soil sample 16 and $< 25\%$ for ii, iii, 1, 6 and 11).

Next, τ_e of soil samples i, ii and iii are compared with the Shields stability criterion (Shields, 1936), for which τ_e is also defined as the extrapolated zero transport rate during time-independent erosion. The Shields stability criterion exhibits an increasing θ and thus increasing erosion threshold with decreasing d_{50} for relatively fine sands ($< 100\,\mu m$). Shields (1936) attributes this to the lower bed roughness of fine-grained beds compared to coarse-grained beds. Fig. 13 shows the critical Shields parameter θ_{cr} $(-)$ as function of the dimensionless particle parameter $d_*[-] = [(s-1)g/v^2]^{1/3}d_{50}$, where s $(-)$ is the relative density (specific sediment density divided by density of water), d_{50} (m) the median particle size of the mixtures and v ($m^2\,s^{-1}$) the kinematic viscosity of water.

A pronounced difference exists between the Shields stability criterion and τ_e presented in the current study. For an increasing silt content, τ_e deviates from the criterion. A similar trend was found by Robberts et al. (1998), who studied the erosion of fine-grained granular mixtures. They report a relation between density and erosion rates for $d_{50} < 222\,\mu m$ ($d_* < 5.6$), whereas for larger d_{50} erosion rates are independent of the density. This indicates that for small grained granular beds bulk characteristics rather than individual particle characteristics become important.

A possible explanation is that the Shields criterion is calibrated for relatively coarse ($> 100\,\mu m$) and well-sorted sediments, which implies that sorting effects are not incorporated. These effects concern a generally denser maximum packing density for poorly sorted mixtures (large d_{90}/d_{10}) compared to well-sorted (small d_{90}/d_{10}) mixtures with similar d_{50}. Denser packing may yield a larger internal friction which enhances τ_e. However, another possibility is that due to a lower permeability (decreases with increasing d_{90}/d_{10}, see e.g. Head, 1980) the dissipation rate of pore water pressure gradients decreases, yielding the importance of apparent cohesion, which augments failure resistance and, therefore, decreases erodibility. This will be subject of further study.
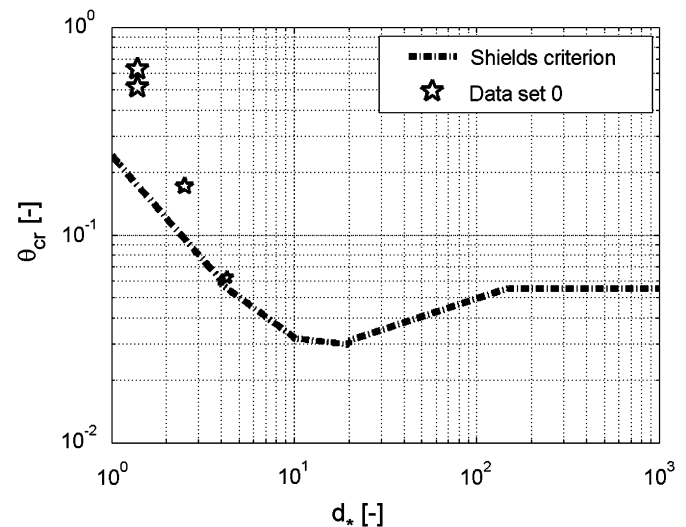

Fig. 13. Shields stability criterion (dash–dotted line) with the critical Shield parameter θ_{cr} as function of the dimensionless particle parameter d_*. Data for soil samples of set 0 ($*$) are shown, for which the size of the markers increases with increase in silt content.

5.5. Undrained shear strength

Generally, sediment strength is expected to increase for increasing ξ_{cl}. This agrees with the behavior of the undrained shear strength for mixtures with a dominant clay–water matrix (Fig. 10). However, the opposite occurs for a dominant sand–silt skeleton. Results shown in Fig. 10 are comparable with those presented by Jacobs et al. (2007a), which only qualitatively explain this contradicting behavior. The current study provides a quantitative explanation, following Van Kesteren (in preparation). First, the two branches in Fig. 10 are individually discussed and a theoretical model is presented to explain the combined effects of a non-cohesive sand–silt skeleton and a cohesive clay–water mixture.

The undrained shear strength of a clay–water matrix depends on the relation between the plasticity and packing density (reflected by W_{rel}), with more clay and/or less water resulting in larger c_u. From results of Jacobs et al. (2007a), a power law relation is proposed (see continuous line in Fig. 10) for c_u of clay–water mixture ($c_{u,clw}$, (Pa)), independently of the clay mineralogy:

$$c_{u,clw} = B_1 W_{rel}^{B_2} \tag{9}$$

where the empirical coefficients B_1 and B_2 are 2770 Pa and -2.5, respectively. It is noted that Eq. (9) enables the comparison of c_u of clay–water mixtures with varying W, ξ_{cl} and/or clay mineralogy.

The behavior of c_u as function of W_{rel} for mixtures with a granular skeleton is explained following Bagnold (1954) and depends on the ratio of the actual and the maximum (densest packing) volume concentration of sand and silt. This ratio is expressed by the linear concentration (λ ($-$), Bagnold, 1954):

$$\lambda = 1/((\phi/\phi_{max})^{-1/3} - 1) \tag{10}$$

where $\phi_{max}(= 1 - n_{sasi,min})$ is the densest volume concentration of a granular skeleton and ϕ the actual concentration. It is noted that λ increases with increasing packing density, and that $n_{sasi,min}$ varies with a varying ratio between the volume fractions of sand and silt (Fig. 1).

The contribution of the granular fraction to c_u increases with increasing λ, and is reflected by an exponential relation (Fig. 14):

$$c_u/c_{u,clw} = e^{\alpha\lambda} \tag{11}$$

where α ($= 0.12$ ($-$)) is an empirical parameter. Fig. 14 shows that all data, including those with bentonite, are nicely fitted with

Eq. (11), which confirms the significance of the granular porosity as a discriminator between a sand–silt skeleton and a clay–water matrix.

Combination of Eqs. (9) and (11) generates a model to predict c_u of sand–mud mixtures as function of W_{rel} and λ:

$$c_u = B_1 W_{rel}^{B_2} e^{\alpha\lambda} \tag{12}$$

The input for this model concerns the minimum concentration of the granular fraction ($n_{sasi,min}$) and the strength of the clay–water mixture ($c_{u,clw}$). Fig. 15 shows that the data are in agreement with the model, and that the cohesive and non-cohesive branches as shown in Fig. 10 are well represented.

Finally, Fig. 16 shows positive correlation between c_u and τ_e for a dominant clay–water matrix, and a negative correlation for a dominant sand–silt skeleton. For a clay–water matrix both the
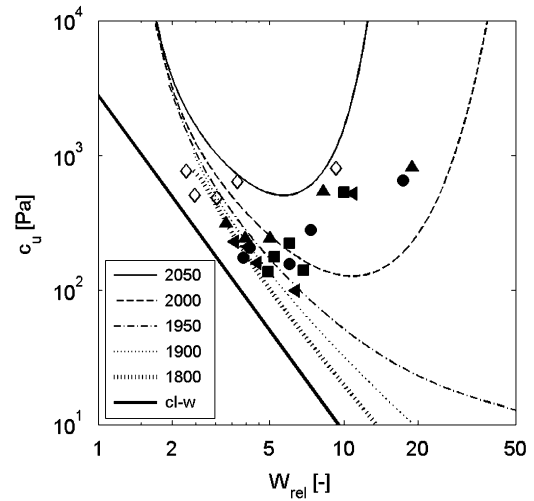
Fig. 15. Modeled c_u as function of W_{rel} (Eq. (12)) for sand–mud mixtures with varying bulk density (see box in the bottom-left corner) and for constant clay–silt ratio (1/4) and clay mineralogy (kaolinite). The diagonal continuous line reflects c_u for mixtures of clay and water only (Eq. (10)). The left and right branches of c_u concern soils with a dominant clay–water matrix and sand–silt skeleton, respectively. Also experimental data for samples of sets 1 (●), 2 (▲), 3 (■), 4 (◄) and 5 (◇) are shown. Note that the experimental samples of one set do not exhibit constant density, which explains why they are not fitted by one of the lines as shown.
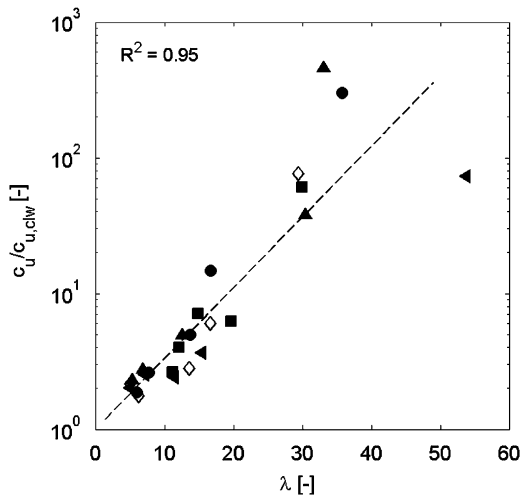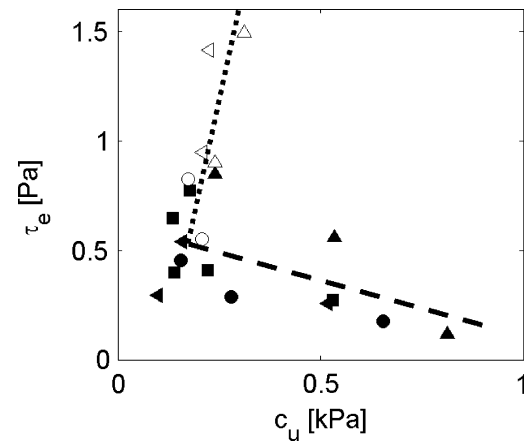

Fig. 14. Total undrained shear strength divided by the undrained shear strength of the granular fraction as function of the linear concentration of sand and silt for samples of sets 1 (●), 2 (▲), 3 (■), 4 (◄) and 5 (◇). The dashed line reflects Eq. (12). Larger λ implies a denser packing of sand and silt.

Fig. 16. Relation between undrained shear strength (c_u) and erosion threshold (τ_e) for sets, 1, 2, 3 and 4. The black-colored markers refer to data for soils with a dominant sand–silt skeleton (fitted with the dashed line); the white-colored markers refer to data for soils with a dominant clay–water matrix (fitted with the dotted line). The dotted line indicates a positive correlation in case of a clay–water matrix and the dashed line a negative correlation in case of a sand–silt skeleton.

drained and the undrained strength increase for increasing clay content as more clay generates stronger cohesive bonding (i.e. larger τ_e), which results in lower W_{rel} and, subsequently, larger c_u (Eq. (9)). For a dominant sand–silt skeleton, τ_e increases for increasing ξ_{cl} due to enhanced cohesive bonding, whereas c_u decreases due to the larger volume concentration of clay and the, subsequently, decreased λ (i.e. looser packing). These correlations confirm the drained character of surface erosion.

6. Conclusions

Results of about 50 erosion tests on soil samples with varying composition in terms of clay–silt and sand–silt ratio and clay mineralogy are presented. Sediment beds exhibit purely granular behavior for a plasticity index smaller than 2. For larger PI^* two types of erosion exist: floc and surface erosion. Floc erosion exists for low bed shear stress. It is a time-decreasing process during which individual mud flocs are randomly eroded. Flocs are already eroded for a bed shear stress larger than zero due to the turbulent fluctuations of the bed shear stress, which indicates the importance of the stochastic character of the flow conditions. Erosion ceases when all erodible flocs are eroded.

For larger bed shear stress time-independent erosion is observed, during which individual sand and mud particles are simultaneously and uniformly eroded. The threshold bed shear stress is defined as the extrapolated zero transport rate. Surface erosion properties are determined by material properties rather than by the stochastic properties of the flow conditions. Current study discusses the surface erosion threshold by applying a geotechnical approach, for which surface erosion is characterized as a drained process. Drained indicates that the time-scale of the forcing conditions are similar to the time-scale of the response of the bed, yielding no pore water pressure gradients. This implies that only the cohesive strength of the sediment bed is important for the surface erosion threshold, rather than the packing density. This geotechnical approach is confirmed by the experimental results.

First, the surface erosion threshold exhibits a negative correlation with the water content, which is a measure for the packing density. However, a clear power law relation exists between the threshold and the plasticity index, which is a bulk material parameter for the cohesiveness of a soil as function of the clay content, the type of clay mineral and the effect pore water chemistry. The power law relation agrees with literature, which is remarkable as soils with varying structures and clay mineralogy are applied.

Second, the erosion threshold for granular mixtures partly agrees with the Shields stability criterion, as for small-grained and poorly sorted mixtures a deviation with this criterion exists. Although more study is required, a possible explanation is that due to the existence of pore water pressure gradients resulting from a decreased permeability, the threshold increases.

Finally, a semi-empirical model is generated for the undrained shear strength of sand–mud mixtures as function of the granular porosity and plasticity, which was validated with experimental data. The comparison of the undrained shear strength with the surface erosion threshold further confirms that the latter exhibits a drained character.

In conclusion, the recognition of time-decreasing and time-independent erosion partly solves the confusion concerning the definition of the erosion threshold. Furthermore, results for artificially generated soil samples confirm the applicability of a geotechnical approach to study the erosion of sediment mixtures. Furthermore, the enhanced insight in the behavior and erosion of artificially generated sand–mud mixtures enables a better

understanding of the behavior of natural sediments. Finally, only the erosion threshold is discussed in this study. In future research, also the erosion rate/erosion parameter as function of sediment composition will be studied.

References

Ariathurai, C.R., 1974. A finite element model for sediment transport in estuaries. Ph.D. Thesis. University of California, Davis.

ASTM D2487, 2006. Standard practice for classification of soils for engineering purposes (unified soil classification system). In: Annual Book of ASTM standards, American Society for Testing Materials, West Conshohocken.

ASTM D4254, 2006. Standard test for minimum index density and unit weight of sils and calculation of relative density. In: Annual Book of ASTM standards, American Society for Testing Materials, West Conshohocken.

ASTM D4318, 2000. Standard test for liquid limit, plastic limit and plasticity index of soils. In: Annual Book of ASTM standards, American Society for Testing Materials, West Conshohocken.

ASTM D4648, 2005. Standard test for laboratory miniature vane shear test for saturated fine-grained clayey soil. In: Annual Book of ASTM Standards, American Society for Testing Materials, West Conshohocken.

Bagnold, R.A., 1954. Experiments on a gravity-free dispersion of large solid spheres in a Newtonian fluid under shear. Proceedings of the Royal Society of London 225 (1160), 49–63.

Flemming, B.W., 2000. A revised textural classification of gravel-free muddy sediments on the basis of ternary diagrams. Continental Shelf Research 20, 1125–1137.

Grass, A.J., 1970. Initial instability of fine bed sand. Journal of the Hydraulics Division 96 (HY3), 619–632.

Head, K.H., 1980. Manual of Soil Laboratory Testing, Volume 1: Soil Classification and Compaction Tests. Pentech Press, London, ISBN: 0-7273-1302-9.

Jacobs, W., Van Kesteren, W.G.M., Winterwerp, J.C., 2007a. Strength of sediment mixtures as a function of sand content and clay mineralogy. In: Kusuda, T., Yamanishi, H., Spearman, J., Gailani, J.Z. (Eds.), Proceedings in Marine Science. Sediment and Ecohydraulics, Intercoh 2005, vol. 9; 2007.

Jacobs, W., Van Kesteren, W.G.M., Winterwerp, J.C., 2007b. Permeability and consolidation of sediment mixtures as function of sand content and clay mineralogy. International Journal of Sediment Research 22 (3), 180–187.

Kandiah, A., 1974. Fundamental aspects of surface erosion of cohesive soils. Ph.D. Thesis. University of California, USA.

Le Hir, P., Cann, P., Waeles, B., Jestin, H., Bassoullet, P., 2006. Instrumentation légère pour la mesure de l'érodabilité des sédiments vaseux ou sablo-vaseux. IXèmes Journées Nationales Génie Côtier-Génie Civil, Brest, 12–14 Septembre 2006 (in French).

Le Hir, P., Cann, P., Waeles, B., Jestin, H., Bassoullet, P., 2007a. Erodability of natural sediments: experiments on sand/mud mixtures from laboratory and field erosion tests. In: Proceedings of the Intercoh 2007 Conference, Saga, Japan: Special issue Marine Science. ISBN: 9780444531841.

Le Hir, P., Monbet, Y., Orvain, F., 2007b. Sediment erodability in sediment transport modelling: can we account for biota effects? Continental Shelf Research 27, 1116–1142.

Panagiotopoulos, I., Voulgaris, G., Collins, M.B., 1997. The influence of clay on the threshold of movement of fine sandy beds. Coastal Engineering 32, 19–43.

Parchure, T.M., Mehta, A.J., 1985. Erosion of soft cohesive sediment deposits. Journal of Hydraulic Engineering 111 (10), 1308–1326.

Partheniades, E., 1962. A study of erosion and deposition of cohesive soils in salt water. Ph.D. Thesis. University of California, Berkeley.

Partheniades, E., 1965. Erosion and deposition of cohesive soils. Journal of the Hydraulics Division 91, 105–139.

Righetti, M., Lucarelli, C., 2007. May the shields theory be extended to cohesive and adhesive benthic sediments? Journal of Geophysical Research, 112.

Roberts, J., Jepsen, R., Gotthard, D., Lick, W., 1998. Effects of particle size and bulk density on erosion of quartz particles. Journal of Hydraulic Engineering 124 (12), 1261–1267.

Sanford, L.P., 2006. Uncertainties in sediment erodibility estimates due to a lack of standards for experimental protocols and data interpretation. Integrated Environmental Assessment and Management 2 (1), 29–34.

Schofield, A.N., Wroth, C.P., 1968. Critical State Soil Mechanics. McGraw-Hill, London.

Shields, A., 1936. Anwendung der Aehnlichkeitsmechanik und der Turbulenzforschung auf die Geschiebebewegung. Mitteilungen der Preußischen Versuchsanstalt für Wasserbau und Schiffbau, Berklin, NW 87.

Skempton, A.W., 1965. The colloidal activity of clay. In: Proceedings of the Third International Conference on Soil Mechanics and Foundation Engineering, vol. I, pp. 57–61.

Smerdon, E.T., Beasley, R.P., 1959. The tractive force theory applied to stability of open channels in cohesive soil. Agricultural Experimental Stability Research Bulletin 715, 1–36.

Torfs, H., 1995. Erosion of mud/sand mixtures. Ph.D. Thesis. Katholieke Universiteit Leuven.

Vanoni, V.A., 1964. Measurements of critical shear stress for entraining fine sediments in a boundary layer. Report No. KH-R-7, W.M. Keck Laboratory for Hydraulics and Water Resources, California Institute of Technology, USA, 47pp.

Van Rijn, L.C., 1993. Principles of sediment transport in rivers, estuaries and coastal seas. Aqua Publications, Amsterdam. ISBN: 9080035629.

Van Prooijen, B.C., Winterwerp, J.C., 2010. A stochastic formulation for erosion of cohesive sediments. Journal of Geophysical Research 115, C01005.

Van Kesteren, W., in preparation. Ph.D. Thesis, University of Technology Delft.

Van Ledden, M., Van Kesteren, W.G.M., Winterwerp, J.C., 2004. A conceptual framework for the erosion behavior of sand–mud mixtures. Continental Shelf Research 24, 1–11.

Winterwerp, J.C., Van Kesteren, W.G.M., 2004. Introduction to the physics of cohesive sediment in the marine environment. Developments in Sedimentology. Elsevier ISBN:0-4444-51553-4.